



Kent Academic Repository

Sun, Jun, Hossain, Md. Moinul, Xu, Chuan-Long, Zhang, Biao and Wang, Shi-Min (2017) *A novel calibration method of focused light field camera for 3-D reconstruction of flame temperature*. *Optics Communications*, 390 . 7 - 15. ISSN 0030-4018.

Downloaded from

<https://kar.kent.ac.uk/67210/> The University of Kent's Academic Repository KAR

The version of record is available from

<https://doi.org/10.1016/j.optcom.2016.12.056>

This document version

Author's Accepted Manuscript

DOI for this version

Licence for this version

UNSPECIFIED

Additional information

Versions of research works

Versions of Record

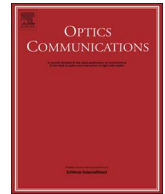
If this version is the version of record, it is the same as the published version available on the publisher's web site. Cite as the published version.

Author Accepted Manuscripts

If this document is identified as the Author Accepted Manuscript it is the version after peer review but before type setting, copy editing or publisher branding. Cite as Surname, Initial. (Year) 'Title of article'. To be published in *Title of Journal*, Volume and issue numbers [peer-reviewed accepted version]. Available at: DOI or URL (Accessed: date).

Enquiries

If you have questions about this document contact ResearchSupport@kent.ac.uk. Please include the URL of the record in KAR. If you believe that your, or a third party's rights have been compromised through this document please see our [Take Down policy](https://www.kent.ac.uk/guides/kar-the-kent-academic-repository#policies) (available from <https://www.kent.ac.uk/guides/kar-the-kent-academic-repository#policies>).



A novel calibration method of focused light field camera for 3-D reconstruction of flame temperature



Jun Sun^a, Md. Moinul Hossain^b, Chuan-Long Xu^{a,*}, Biao Zhang^a, Shi-Min Wang^a

^a Key Laboratory of Energy Thermal Conversion and Control of Ministry of Education, School of Energy and Environment, Southeast University, Nanjing 210096, China

^b School of Engineering and Digital Arts, University of Kent, Canterbury, Kent CT2 7NT, UK

ARTICLE INFO

Keywords:

Focused light field camera
Camera calibration
3-D reconstruction
Flame temperature

ABSTRACT

This paper presents a novel geometric calibration method for focused light field camera to trace the rays of flame radiance and to reconstruct the three-dimensional (3-D) temperature distribution of a flame. A calibration model is developed to calculate the corner points and their projections of the focused light field camera. The characteristics of matching main lens and microlens f-numbers are used as an additional constrains for the calibration. Geometric parameters of the focused light field camera are then achieved using Levenberg-Marquardt algorithm. Total focused images in which all the points are in focus, are utilized to validate the proposed calibration method. Calibration results are presented and discussed in details. The maximum mean relative error of the calibration is found less than 0.13%, indicating that the proposed method is capable of calibrating the focused light field camera successfully. The parameters obtained by the calibration are then utilized to trace the rays of flame radiance. A least square QR-factorization algorithm with Plank's radiation law is used to reconstruct the 3-D temperature distribution of a flame. Experiments were carried out on an ethylene air fired combustion test rig to reconstruct the temperature distribution of flames. The flame temperature obtained by the proposed method is then compared with that obtained by using high-precision thermocouple. The difference between the two measurements was found no greater than 6.7%. Experimental results demonstrated that the proposed calibration method and the applied measurement technique perform well in the reconstruction of the flame temperature.

1. Introduction

Flame is a 3-D medium with sparse density, particle participation and self-illumination. It plays an essential role in various industrial processes such as combustion in power plant and rocket engine. Where temperature is one of the most important characteristic parameters of the flame and closely linked to the performance of the combustion process. In the process of combustion diagnostics, the quantitative characterization of flame temperature can be used for informing the operators or the control system to diagnose the state of the flame or to optimize the process [1]. However, the 3-D temperature measurement is then crucial for improving the combustion efficiency and controlling the product such as NO_x [2–4]. Besides, to achieve an in-depth understanding of combustion processes, the spatial and temporal measurement of the flame temperature in a combustion system is also necessary and an effective means for the 3-D measurement of flame temperature remains a challenge for combustion engineers and researchers [5,6]. Over the past few years various measurement techni-

ques were developed to reconstruct the temperature distribution of a flame, such as laser based diagnostics techniques [7–10], single camera [11–13] and multi-cameras based diagnostics techniques [5,6,14–16]. For example, Doi et al. [8] reconstructed the 3-D temperature distribution of turbulent flame using multi-directional holographic interferograms. Ma et al. [9] proposed a novel technique to obtain simultaneous tomographic images of flame temperature and species concentration based on hyperspectral absorption spectroscopy. Yang et al. [10] presented the water vapour multiplexed tunable diode-laser absorption spectroscopy (TDLAS) technique to obtain the 3-D flame temperature. However, laser based diagnostics techniques require more complex system and unsuitable for industrial furnaces due to the complex setup, high cost of the system. A single CCD (charge-coupled device) camera or multi-cameras based tomographic techniques [5,6,11–16] are also used for the 3-D temperature measurements. For instance, Huang et al. [11] proposed a method to reconstruct the soot temperature and volume fraction of the flame sections. LSQR (least square QR-factorization algorithm) algorithm and two-color

* Corresponding author.

E-mail address: chuanlongxu@seu.edu.cn (C.-L. Xu).

technique with a single camera based stereoscopic image system were used. Brisley et al. [13] developed a prototype instrumentation system based on two-color pyrometry and image processing techniques to reconstruct the 3-D flame temperature using a single CCD camera. Those techniques are simple in structure and thus being easy to install on a practical furnace but they can only be used under strict condition such as a high level of rotational symmetry and stable flames. Recently, Hossain et al. [5] developed an optical tomographic algorithm incorporating logical filtered back-projection and simultaneous algebraic reconstruction techniques to reconstruct the grey-level intensities of flame sections using optical imaging fiber bundles and multi-cameras based imaging system. The flame temperature is determined from the reconstructed grey-level intensities based on the two-color principle. Gong et al. [14] proposed a new combination of optical sectioning tomography (OST) and two-color method to reconstruct the 3-D temperature distribution of impinging flames in an opposed multi-burner gasifier. Though a more reliable and accurate 3-D temperature reconstruction of flames can be achieved using the multi-cameras systems compared to single camera systems. But they are in high system cost, complexity in system setup and installation. Besides, Li et al. [16] proposed a radiative imaging model and Tikhonov regularization method to reconstruct the 3-D flame temperature field. However, these techniques (single camera or multi-cameras based techniques) utilized the conventional CCD camera which is unable to distinguish the direction of flame radiance and hence the radiance of flame captured by a conventional camera is limited to two-dimensional (2-D). Whereas the light field camera is capable of recording the direction of each ray with corresponding intensity and 3-D radiance field of the flames through a single exposure [17–20]. And the cone angle of the flame radiance captured by a single pixel of a light field camera is much smaller than that of a conventional camera [21].

In recent years, the application of the light field camera is increasing with the maturing of the manufacturing technique of microlens array [22–28]. To determine the 3-D position of the object, the geometric calibration of the focused light field camera is important. It is also crucial to obtain the intrinsic parameters (such as separation between the main lens and the CCD sensor) of the light field camera for related applications like ray tracing. However, very limited research can be found on the geometric calibration of the focused light field camera, particularly for the 3-D temperature reconstruction of a flame [21,29]. Jeffrey et al. [29] preliminarily investigated the 3-D measurement of flames with a light field camera using image refocusing, 3-D deconvolution and tomographic reconstruction techniques. However, feasible methods were not proposed to reconstruct the flame temperature or to calibrate the focused light field camera. Sun et al. [21] also preliminarily reconstructed the 3-D temperature distributions of the flame using a single light field camera where the geometric calibration of the focused light field camera was not considered. Usually, the relationship between the 3-D point on calibration board and the image point on the sensor plane for main lens is utilized to calibrate the conventional camera [30–32]. Because the corner points are imaged twice by the main lens and microlenses in the focused light field camera, these methods for conventional camera [30–32] cannot be employed directly to calibrate the focused light field camera. Yunsu et al. [33] developed an efficient geometric calibration method for traditional light field camera (i.e. lytro light field camera) using line features technique. Basically distance between the sensor plane and the microlens array in the lytro light field camera is equal to the focal length of each microlens. Hence the 3-D point on calibration board is not imaged directly on the sensor [33]. It is therefore difficult to extract precise locations of the corner points from raw images captured by the lytro light field camera. To capture the positional information of the light field more densely, the microlenses are focused on the image produced by the main lens in the focused light field camera [34–37]. In the focused light field camera the corner points are imaged on virtual image plane by main lens and then re-imaged on the CCD sensor by the

microlenses. The points are thus recognizable on the raw image captured by a focused light field camera while there are no recognizable corner points in the raw image captured by a traditional light field camera. The recognized corner points can then be used for the calibration process. So the line features are not necessary for the geometric calibration of the focused light field camera. The calibration model proposed in [33] is not applicable for the focused light field camera since the CCD sensor deviates from the focal plane of the microlenses. Ole et al. [34] proposed a calibration method for the focused light field camera and the parameters are estimated by minimizing the residual between the projected model points and the measured points of calibration pattern. A sequential quadratic programming (SQP) algorithm was employed to optimize the residual. However, a good initialization of the unknown parameters is required for the accurate optimization, or the algorithm may be converged to local optima. Klaus et al. [35] employed the total focused images to calibrate the focused light field camera. The total focused image is the image which is rendered from the raw image captured by the light field camera and each point in the total focused image is on focus. Generally, a clear total focused image relies on a series of reliable algorithms (e.g., refocusing algorithm). The calibration method described in [35] is then capable of calibrating the focused light field camera with high accuracy. However, the relationship between the virtual image points and their projections for microlenses is not included in their calibration model. The preliminary geometric calibration of the focused light field camera using raw light field images was presented in [37]. But the method was performed very poor and the high reprojection errors was found up to 1.8%. The overall optimization was also not considered in the calibration procedures.

This paper presents a novel geometric calibration method of focused light field camera with overall optimization in the calibration procedures and the evaluation of the 3-D reconstruction of flame temperature. The developed geometric calibration model is solved by incorporating the Levenberg-Marquardt algorithm. To establish the calibrations, the same f-numbers of main lens and microlens are applied. The calibrations of a focused light field camera are performed by using a bespoke calibration board. Results obtained from the calibration are presented and analyzed. Experiments were carried out on a lab-scale ethylene air fired combustion test rig to reconstruct the 3-D temperature distribution of a flame. The results obtained from the experiments are presented and discussed. Flame temperature was also measured by thermocouple and compared with the reconstructed temperature of the flame and their results are described.

2. Methodology

2.1. Proposed geometric calibration model

Fig. 1 illustrates the schematic diagram of radiative imaging model of the flame based on a single focused light field camera. In this model,

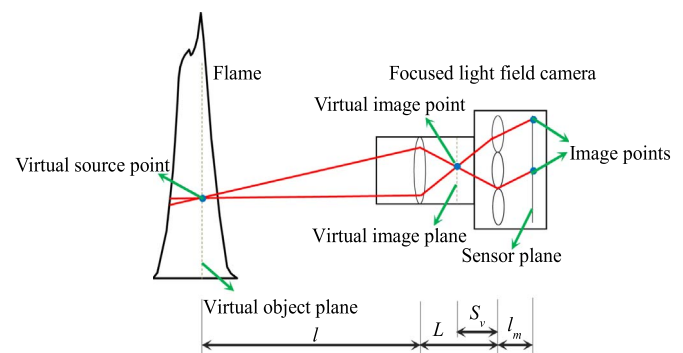


Fig. 1. Schematic diagram of the radiative imaging model of the focused light field camera.

l_m and S_v are the distances from the microlens array to CCD sensor plane and to virtual image plane, respectively. L and l are the distances from main lens to the microlens array and to the virtual object plane, respectively. The virtual image plane is the conjugate plane of the CCD sensor for microlenses. The virtual object plane of the light field camera is the conjugate plane of the virtual image plane for the main lens. The point on virtual image plane is called the virtual image point and the point on virtual focal plane is called the virtual source point. The rays emitted by one virtual source point are converged to the virtual image point by main lens and then re-converged to the pixels (i.e. image points) of the sensor by the microlenses in the focused light field camera [17,18].

In order to trace the directions of the rays of flame radiance, it is required to calibrate the geometric parameters (L , l_m , S_v) of the focused light field camera. Basically, the focused light field camera consists of two layers of lenses: the main lens and the microlens array. For the lenses, pinhole camera model is applied to construct the calibration model. Defining the camera coordinate system, the principal point of the main lens is taken as the origin, x and y axes are parallel to image plane, and z axis is perpendicular to image plane. The image coordinate system takes the center of the CCD sensor plane as the origin, x , y and z axes are parallel to that of the camera coordinate system. The world coordinate system is defined based on the calibration board, x and y axes are parallel to the board, and z axis is perpendicular to the board. The relationship of the corner point (\mathbf{M}), the virtual image point (\mathbf{m}') and the image point (\mathbf{m}) are obtained, as shown in Fig. 2. The camera coordinates of the virtual image point can be expressed by

$$V_x = \frac{S_v}{l_m} \left(x - \left(1 + \frac{l_m}{S_v} \right) M_x \right) = -\frac{(L - S_v)}{Z_c} X_c \quad (1)$$

where x , M_x and X_c are the x camera coordinates of the image point, center of the corresponding microlens, virtual image point and corner point, respectively. Z_c is the spacing between the calibration board and the main lens.

Similar to calibration model of conventional camera [31], the transformation formula Eq. (2) of the corner point (\mathbf{M}) and its image projection (\mathbf{m}') is obtained. The corresponding coordinate vectors ($\widetilde{\mathbf{m}}'$, $\widetilde{\mathbf{M}}$) of the virtual image point and the corner point are expressed by Eqs. (3) and (4). Note that the raw light field images are employed for calibration, the coordinate vector ($\widetilde{\mathbf{m}}'$) is obtained from the coordinate of the image point (\mathbf{m}). The ratio of l_m/S_v (i.e. β_m) is calculated using Eq. (5) according to the relationship between the virtual image point (\mathbf{m}') and its projected image points (\mathbf{m}_1 and \mathbf{m}_2) and shown in Fig. 2. The intrinsic matrix \mathbf{A} of the focused light field camera is given by Eq. (6) and the parameters α , β and γ are described by Eqs. (7–9).

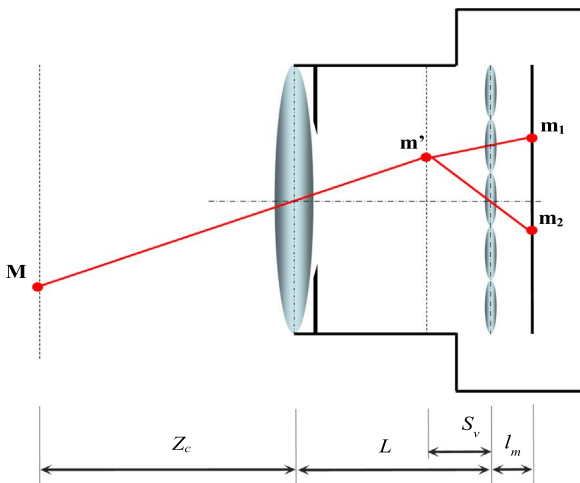


Fig. 2. Schematic diagram of the calibration model of the focused light field camera.

$$s\widetilde{\mathbf{m}}' = \mathbf{A}[\mathbf{R} \ \mathbf{t}]\widetilde{\mathbf{M}} \quad (2)$$

$$\widetilde{\mathbf{m}}' = \left[-\frac{S_v}{l_m} \left(u - \left(1 + \frac{l_m}{S_v} \right) M_u \right), -\frac{S_v}{l_m} \left(v - \left(1 + \frac{l_m}{S_v} \right) M_v \right), 1 \right]^T \quad (3)$$

$$\widetilde{\mathbf{M}} = [X, Y, Z, 1]^T \quad (4)$$

$$\beta_m = \frac{l_m}{S_v} = \frac{u_1 - u_2}{M_{u1} - M_{u2}} - 1 \quad (5)$$

$$\mathbf{A} = \begin{bmatrix} \alpha & \gamma & u_0 \\ 0 & \beta & v_0 \\ 0 & 0 & 1 \end{bmatrix} \quad (6)$$

$$\alpha = \frac{L - S_v}{dx} \quad (7)$$

$$\beta = \frac{L - S_v}{dy} \quad (8)$$

$$\gamma = \frac{(L - S_v)\tan a}{dy} \quad (9)$$

where s is an arbitrary scale factor and it depends on the distance between the camera and the calibration board. And the extrinsic parameters (\mathbf{R} , \mathbf{t}) are the rotation and translation vectors which relate the world coordinate system to the camera coordinate system [38]. u_1 and u_2 are the image coordinates in pixels of the two image points (\mathbf{m}_1 and \mathbf{m}_2), respectively. M_{u1} and M_{u2} are the image coordinates in pixels of the centers of the corresponding microlenses, respectively. dx and dy are the sizes of the pixel of the CCD sensor and they are assumed to be known in the calibration model. a denotes the angle of skewness of two image axes. u_0 and v_0 are the image coordinates in pixels of the principal point of the lens, α and β are the scale factors of u and v axes of the image, and γ is the parameter describing the skewness of the two image axes.

Total focused images are also applied to the calibration model Eq. (2) by replacing the calculated coordinates of \mathbf{m}' in Eq. (3) with the coordinates of detected corner points on these images. They are used as a comparison to evaluate the accuracy of the calibration results. To solve the calibration model, Eq. (10) of matching main lens and microlens f-numbers is utilized. Relative sizes of the main lens and microlens apertures are optimized so that the sub-images under each microlens are as large as possible, and have no overlapping in the light field camera [19]. In this case, the f-numbers of the main lens and microlens are equal.

$$\frac{L}{D} = \frac{l_m}{d} \quad (10)$$

where D and d are the diameters of the main lens and microlens apertures, respectively. Note that the f-number of the lens refers to the image-side f-number.

2.2. Light field camera calibration

Once several images of the calibration board under different orientations (more than three in general) are captured by the focused light field camera by moving the plane, the intrinsic parameters (α , β , γ , u_0 and v_0) and extrinsic parameters (three transformation vectors, \mathbf{r}_1 , \mathbf{r}_2 , \mathbf{r}_3 and one translation transformation vector, \mathbf{t}) are determined by using Eq. (2) through following steps. The optimization of intrinsic and extrinsic parameters are processed to improve the calibration accuracy through final refinement (refer to step 4) based on the whole corner points in all utilized images.

- 1) The corner point (\mathbf{M}) and its projection (\mathbf{m}') is related by a homography (\mathbf{H}) which is equal to $\lambda\mathbf{A}[\mathbf{r}_1 \ \mathbf{r}_2 \ \mathbf{t}]$ (λ is an arbitrary scalar). Compute the homography for each image using the maximum likelihood estimation with the Levenberg-Marquardt

Algorithm [32,39].

- 2) The i -th column of matrix \mathbf{H} is assumed to be $[h_{i1}, h_{i2}, h_{i3}]^T$. Mount the matrix \mathbf{V} according to the orthogonality of \mathbf{r}_1 and \mathbf{r}_2 using Eqs. (11) and (12). Compute the eigenvector \mathbf{b} of $\mathbf{V}^T\mathbf{V}$ associated with the smallest eigenvalue and obtain the estimation of $[B_{11}, B_{12}, B_{22}, B_{13}, B_{23}, B_{33}]$.

$$\mathbf{V}_{ij} = [h_{i1}h_{j1}, h_{i1}h_{j2} + h_{i2}h_{j1}, h_{i2}h_{j2}, h_{i3}h_{j1} + h_{i1}h_{j3}, h_{i3}h_{j2} + h_{i2}h_{j3}, h_{i3}h_{j3}]^T \quad (11)$$

$$\mathbf{V} = \begin{bmatrix} \mathbf{V}_{12}^T \\ (\mathbf{V}_{11} - \mathbf{V}_{22})^T \end{bmatrix} \quad (12)$$

- 3) Compute the intrinsic parameters from vector \mathbf{B} using Eqs. (13)–(18) and compute the extrinsic parameters from matrices \mathbf{A} and \mathbf{H} using Eqs. (19)–(22).

$$v_0 = (B_{12}B_{13} - B_{11}B_{23})/(B_{11}B_{22} - B_{12}^2) \quad (13)$$

$$\lambda = B_{33} - [B_{13}^2 + v_0(B_{12}B_{13} - B_{11}B_{23})]/B_{11} \quad (14)$$

$$\alpha = \sqrt{\lambda/B_{11}} \quad (15)$$

$$\beta = \sqrt{\lambda B_{11}/(B_{11}B_{22} - B_{12}^2)} \quad (16)$$

$$\gamma = -B_{12}\alpha^2\beta/\lambda \quad (17)$$

$$u_0 = \gamma v_0/\beta - B_{13}\alpha^2/\lambda \quad (18)$$

$$\mathbf{r}_1 = \lambda \mathbf{A}^{-1} \mathbf{h}_1 \quad (19)$$

$$\mathbf{r}_2 = \lambda \mathbf{A}^{-1} \mathbf{h}_2 \quad (20)$$

$$\mathbf{r}_3 = \mathbf{r}_1 \times \mathbf{r}_2 \quad (21)$$

$$\mathbf{t} = \lambda \mathbf{A}^{-1} \mathbf{h}_3 \quad (22)$$

- 4) Refine all the above parameters by minimizing Eq. (23) with Levenberg-Marquardt Algorithm. k_1 and k_2 are the coefficients of the radial distortion of the main lens [40]. M and n denote the number of corner points in each image and the number of images, respectively. In this study, the initial guess of them are set to zero and the initial guess of \mathbf{A} and $[\mathbf{R} \ \mathbf{t}]$ are calculated in step 3.

$$\sum_{i=1}^n \sum_{j=1}^m \|\mathbf{m}_{ij} - \mathbf{m}(\mathbf{A}, k_1, k_2, \mathbf{R}_i, \mathbf{t}_i, \mathbf{M}_j)\|^2 \quad (23)$$

- 5) Combine the Eqs. (5) and (7) with Eq. (10) for further compute of L , l_m and S_v using Eqs. (24)–(26). Then all the parameters which are required to trace the rays of flame radiation are derived finally.

$$l_m = \frac{\alpha \, dx \, d \beta_m}{D\beta_m - d} \quad (24)$$

$$S_v = l_m/\beta_m \quad (25)$$

$$L = S_v + \alpha \, dx \quad (26)$$

2.3. Temperature measurement technique

The directions in 3-D space of the detected rays can be traced from the camera to the flame accurately based on simple camera pinhole model [21,41]. The detailed radiation calibration procedure and ray tracing procedure can be found elsewhere in [21]. The radiation intensity of the ray of flame radiance is obtained from the grey value of the flame image using blackbody calibration. A pre-calibrated blackbody furnace (LANDCAL R1500T) is utilized to calibrate the radiation intensity.

The relationship between the intensity of the rays of flame radiance and the flame voxels are established using Eq. (27) [42,43].

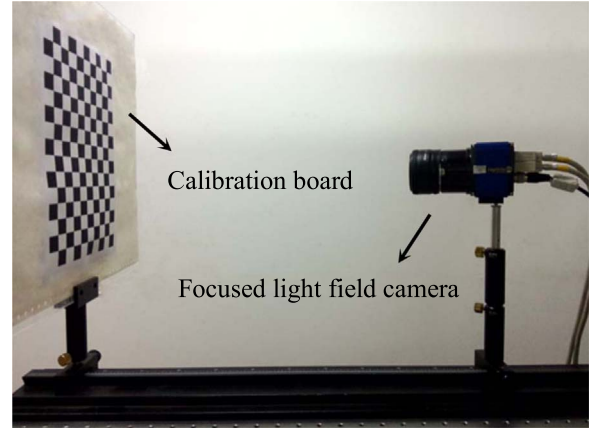


Fig. 3. Physical implementation of the geometric calibration of the focused light field camera.

$$\mathbf{I}_{\text{ccd}} = \mathbf{A} \ \mathbf{I} \mathbf{B}_\lambda \quad (27)$$

where \mathbf{I}_{ccd} is the matrix of the flame intensity distribution on the CCD sensor. $\mathbf{I} \mathbf{B}_\lambda$ is the matrix of all flame voxels. It can be calculated with the monochromatic intensity of blackbody radiation. \mathbf{A} is the coefficient matrix related to the optical thickness. LSQR algorithm is used to solve Eq. (27) and to receive the monochromatic intensity of blackbody radiation $I_{b\lambda}$ of each flame voxel [44]. The temperature T of each flame voxel is then calculated using Eq. (28) according to Planck's law.

$$T = c_2/\lambda \ln [c_1/(\lambda^5 \pi I_{b\lambda} + 1)] \quad (28)$$

where c_1 is the first radiation constant, $3.7418 \times 10^{-16} \text{ W m}^2$ and c_2 is the second radiation constant, $1.4388 \times 10^{-2} \text{ m K}$. λ is the wavelength of the ray, which is 610 nm in this study.

2.4. Calibration setup

For the calibration, a bespoke calibration board (210 mm×297 mm) is designed with 15×9 corner points on the board and placed on the same track with the focused light field camera, as shown in Fig. 3. The board can be rotated and tilted around the support to obtain the images under different angles. A focused light field camera [(R29, Raytrix KAI-29050) interline CCD color image sensor] is used for the calibration. The number of microlens array of the camera is 207×160. The camera has a resolution of 6576(H)×4384(V) and the size of each pixel is 5.5×5.5 μm. The focal length of the main lens is 50 mm. The diameter of the aperture of the main lens is 14 mm and the diameter of each microlens is 165 μm.

2.5. Validation of virtual image points

Fig. 4(a) shows the raw image of the calibration board with image points (marked by yellow stars). Two image points of each corner point can be seen in the figure and all the corresponding virtual image points are then calculated using Eq. (5). The virtual image points are treated as the input data to solve Eq. (4). To investigate the accuracy of the calculated virtual image points, the total focused images are obtained using RxLive software of the camera. The total focused images are calculated using the rendering algorithms [18] which are based on the microlens array with three kinds of focal lengths. They are considered with less noise level of the virtual image points compared to the calculated ones using Eq. (5). As shown in Fig. 4(b), the detected points (marked by yellow stars) are the virtual image points of corresponding corner points on the calibration board. Fig. 5 depicts the differences between the calculated and the detected virtual image points in horizontal and vertical directions. It has been found that the differences of the corner points are no more than 35 pixels in horizontal direction and no more than 25 pixels in vertical direction. Results obtained from

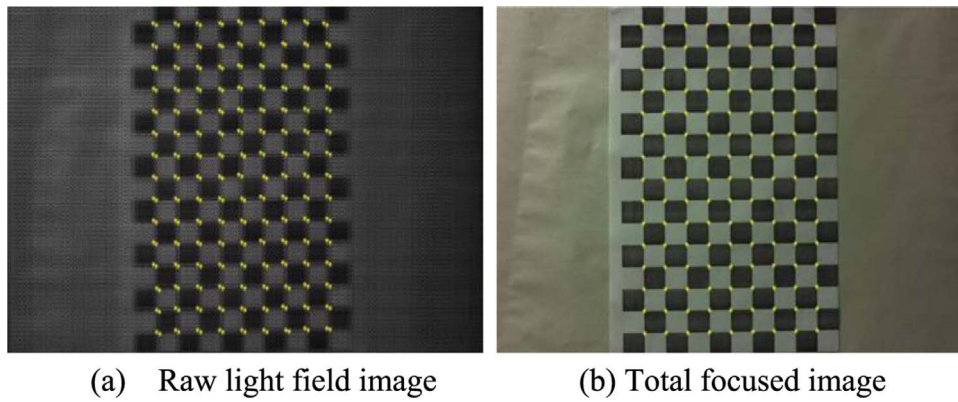


Fig. 4. Images of the calibration board.

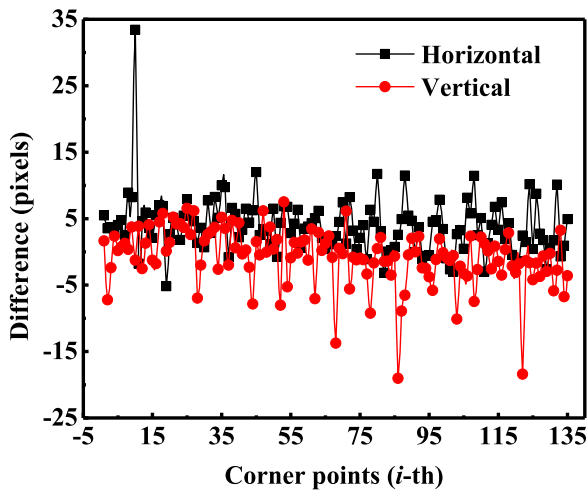


Fig. 5. The difference between the calculated virtual image points from raw light field image and the detected virtual image points from total focused image.

the calibration indicated that the proposed calibration method [refer to Section 2.3] is capable of calculating the virtual image points of the raw images.

2.6. Calibration results

To calibrate the focused light field camera, five raw images of the calibration board under different orientations were captured. The calibrated parameters of the camera are listed in Table 1 and Table 2. Table 1 summarizes the intrinsic parameters of the focused light field camera. The resolution of the CCD sensor is 4384 (H) × 6576 (V) and so the image coordinates of the principal points are supposed to be half of them [i.e., 2192 (H) × 3288 (V)]. The calibrated values of u_0 and v_0 are obtained 2251.4 and 3320.8, respectively and it can be seen that they are close to half of the image coordinate values of 2192 (H) and 3288 (V) with deviations of 2.7% and 0.2%, respectively. In Tables 1 and 2, the negative value of S_v indicates that the virtual image plane and CCD sensor plane are on the same side of the microlens array. Therefore the distance l_m from the sensor to the microlens array is less than the focal length of the microlens array. It has been found that the distance from the main lens to the virtual image plane ($L - S_v$) is 50.1927 mm. This value is also very close to the focal length (50 mm)

Table 1
Intrinsic parameters of the focused light field camera.

| u_0 (pixels) | v_0 (pixels) | l_m (mm) | S_v (mm) | L (mm) |
|----------------|----------------|------------|------------|----------|
| 3320.8 | 2251.4 | 0.5581 | -2.8359 | 47.3568 |

Table 2
Extrinsic parameters of the focused light field camera.

| Image | t (mm) | $r1$ | $r2$ | $r3$ | s (mm) |
|-------|----------|---------|---------|---------|----------|
| 1 | -136.50 | 0.8966 | -0.2377 | 0.3736 | 681.87 |
| | 157.41 | -0.2593 | -0.9658 | 0.0077 | |
| | 681.87 | 0.3590 | -0.1038 | -0.9276 | |
| 2 | -139.42 | 0.9213 | -0.0799 | -0.3805 | 865.08 |
| | 130.82 | 0.0112 | -0.9728 | 0.2314 | |
| | 865.08 | -0.3887 | -0.2175 | -0.8953 | |
| 3 | -152.93 | 0.9691 | -0.2465 | 0.0112 | 760.69 |
| | 165.03 | -0.2385 | -0.9471 | -0.2147 | |
| | 760.69 | 0.0635 | 0.2054 | -0.9766 | |
| 4 | -123.23 | 0.8642 | 0.0800 | 0.4968 | 659.82 |
| | 93.55 | -0.0550 | -0.9664 | 0.2513 | |
| | 659.82 | 0.5002 | -0.2445 | -0.8307 | |
| 5 | -157.74 | 0.9790 | -0.0143 | -0.2034 | 816.08 |
| | 117.92 | -0.0106 | -0.9998 | 0.0192 | |
| | 816.08 | -0.2037 | -0.0166 | -0.9789 | |

of the main lens with a deviation of 0.4%. Table 2 shows the extrinsic parameters corresponding to each image of the calibration board. These parameters describe the positional relation between the camera and the calibration board. The calculated value of s indicates the distance in axial direction between the principal plane of the main lens and the calibration board. The position of the principal plane is then determined according to the calibrated value of s and shown in Fig. 6.

In order to evaluate the accuracy of the calibration, the differences between the virtual image points and the reprojected ones are also calculated. Fig. 7 shows the differences of the corner points on one image of the calibration board. It can be seen that the differences are observed no more than 20 pixels when the raw light field images are used. For the total focused images the differences are also found no

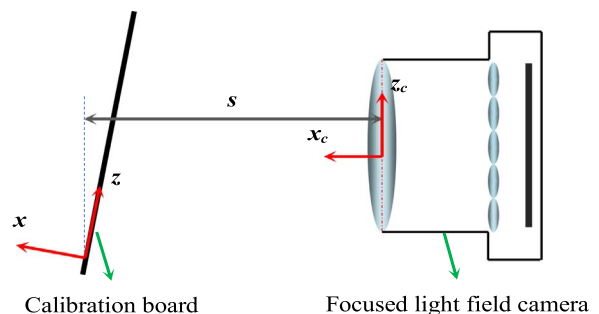
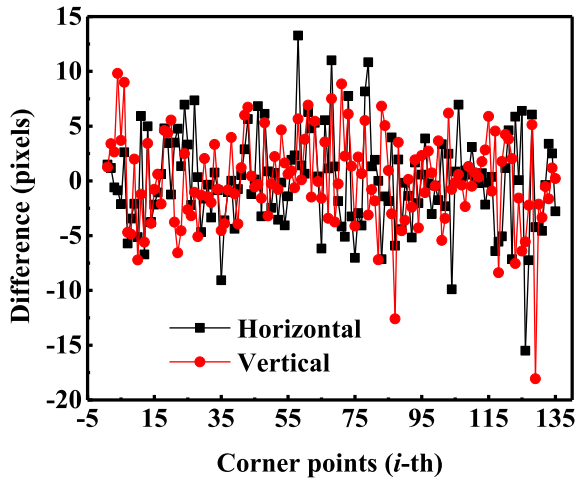
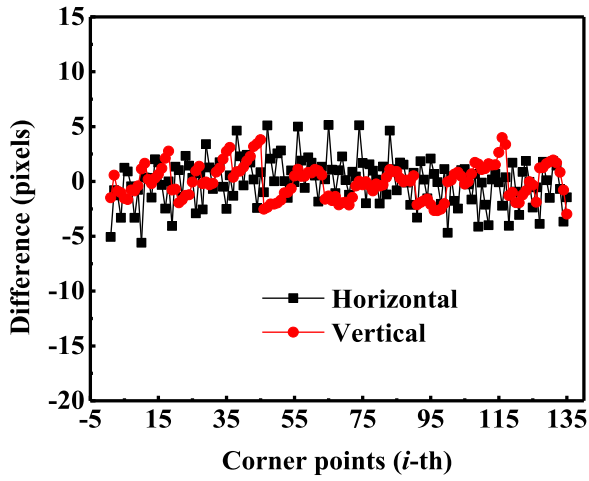


Fig. 6. Schematic diagram of distance between the principal plane of the main lens and the calibration board in axial direction.



(a) Raw light field images



(b) Total focused images

Fig. 7. The differences between the virtual image points and the reprojected virtual image points.

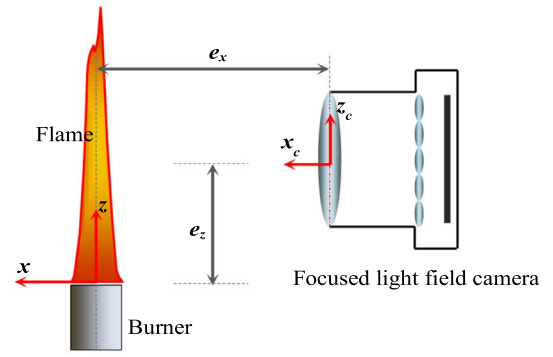
more than 10 pixels. The distances in pixels between the virtual image points and the reprojected virtual image points are calculated using the calibrated parameters. Table 3 summarizes the calculated mean and maximum re-projection errors. The re-projection errors of the calibration for raw light field images and total focused images are less than 36 pixels and 6 pixels, respectively. It can be seen that the proposed calibration method has improved the re-projection errors by 23 pixels and improved the accuracy of 1.67% compared to [36].

The re-projection errors of the calibration results from raw light field images are found more than that from total focused images. This is due to the fact that the accuracy of the calibration is decreased with the increased noise level of virtual image points from raw light field images [refer to Eq. (7)]. The maximum relative error for the raw light field

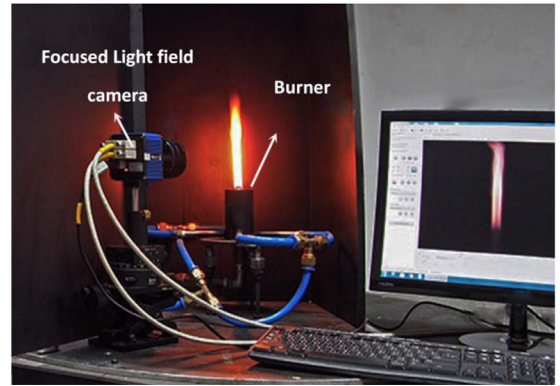
Table 3

Reprojection errors of the calibration.

| Image | Mean Error (pixels) | | Maximum Error (pixels) | | RMS (pixels) | | Mean Relative Error (%) | |
|-------|---------------------|---------------|------------------------|---------------|--------------|---------------|-------------------------|---------------|
| | Raw image | Focused image | Raw image | Focused image | Raw image | Focused image | Raw image | Focused image |
| 1 | 4.0407 | 1.5181 | 41.8509 | 4.7051 | 5.7396 | 1.8323 | 0.1229 | 0.0462 |
| 2 | 3.4243 | 1.4606 | 18.0657 | 5.5932 | 4.5013 | 1.8538 | 0.1041 | 0.0444 |
| 3 | 3.9431 | 1.5104 | 35.5954 | 4.7816 | 5.5695 | 1.8082 | 0.1199 | 0.0459 |
| 4 | 3.7471 | 1.6596 | 24.9994 | 5.9742 | 4.9985 | 1.9939 | 0.1140 | 0.0505 |
| 5 | 3.5692 | 1.5293 | 20.2278 | 5.322 | 4.6221 | 1.8385 | 0.1086 | 0.0465 |



(a) The shift between the flame and camera coordinate system



(b) Physical implementation

Fig. 8. Schematic diagram of the flame and camera coordinate systems (a) and the physical implementation of the flame imaging system (b).

images has been found less than 0.13%. It can therefore be concluded that the proposed calibration model is capable of calibrating the geometric features of a focused light field camera.

3. 3-D Reconstruction of flame temperature

3.1. Experimental setup

The calibrated focused light field camera is placed on one side of the flame to capture the flame images. A co-flow burner is used in this study and more details can be found in [21]. This burner is comprised of an inner tube and an external tube. The inner tube is for fuel flow and the external one is for air flow. The diameters of the inner and external tubes are 12 mm and 50 mm, respectively. The space between the two tubes has an insert of glass bead with the diameter 3 mm and mesh to minimize the flow non-uniformities. To eliminate the influence of ambient light or light reflected, the burner is placed inside a chamber with the black background. In this experiment, the exposure time of the light field camera was set to 0.8 ms and it has been found that the captured flame images are not too dark and not saturated.

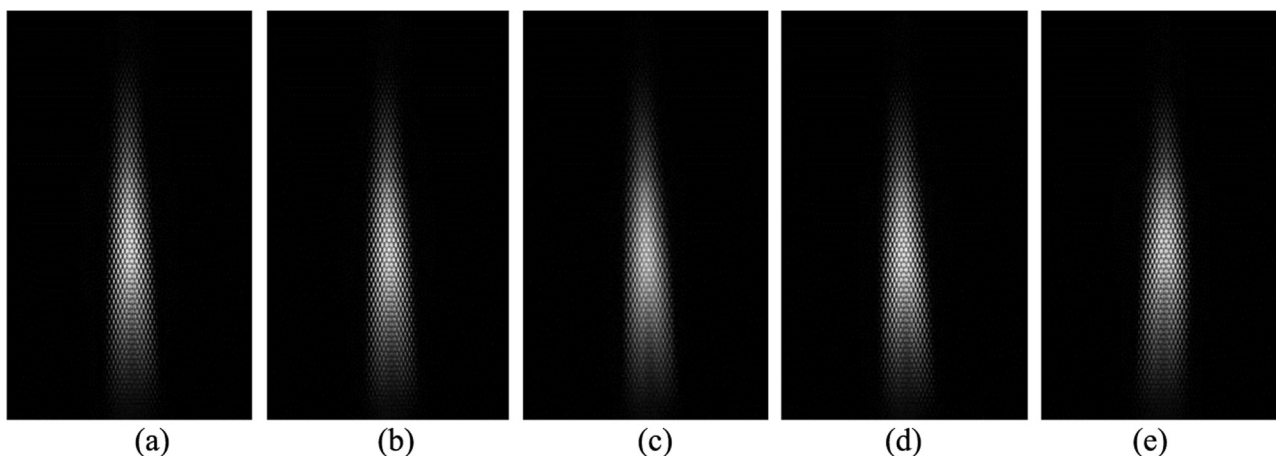


Fig. 9. Example of 2-D flame images captured by the focused light field camera.

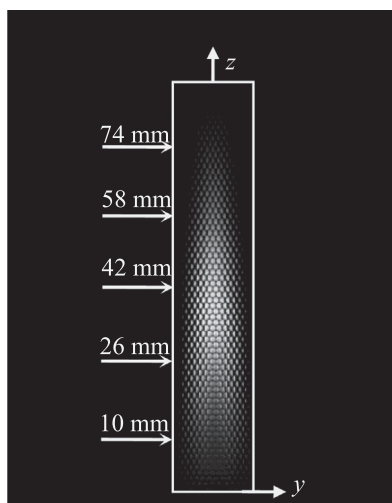


Fig. 10. Raw light field image of the flame.

The flame coordinate system is defined as the camera coordinate system by a shift (e_x, e_y, e_z) of the origin point. This shift is obtained according to the position of the principal plane of the main lens and is shown in Fig. 8(a). In this figure, the origin of the flame coordinate system was set to the center of flame bottom. Experiments were conducted on an ethylene-air fired combustion rig to reconstruct the temperature distribution of flames. The physical experimental setup is shown in Fig. 8(b). In the experiment, the volumetric flow rates of fuel and air are supplied 3 mL/s and 0.1 L/s, respectively and air-fuel ratio was set to 2.38. Fifty flame images were recorded as a raw for this condition. Fig. 9 shows a typical set of 2-D flame images which were taken by the experimental setup. The diameter (root part of the flame) and the height of the flame are calculated 10 mm and 90 mm, respectively. In this study the flame is divided into $1 \times 4 \times 5$ voxels in circumferential, radial direction and axial direction.

3.2. Reconstruction of flame temperature

Once the ethylene-air diffusion flame images are recorded and five cross-sections of the flame are selected from 10 mm to 90 mm in axial

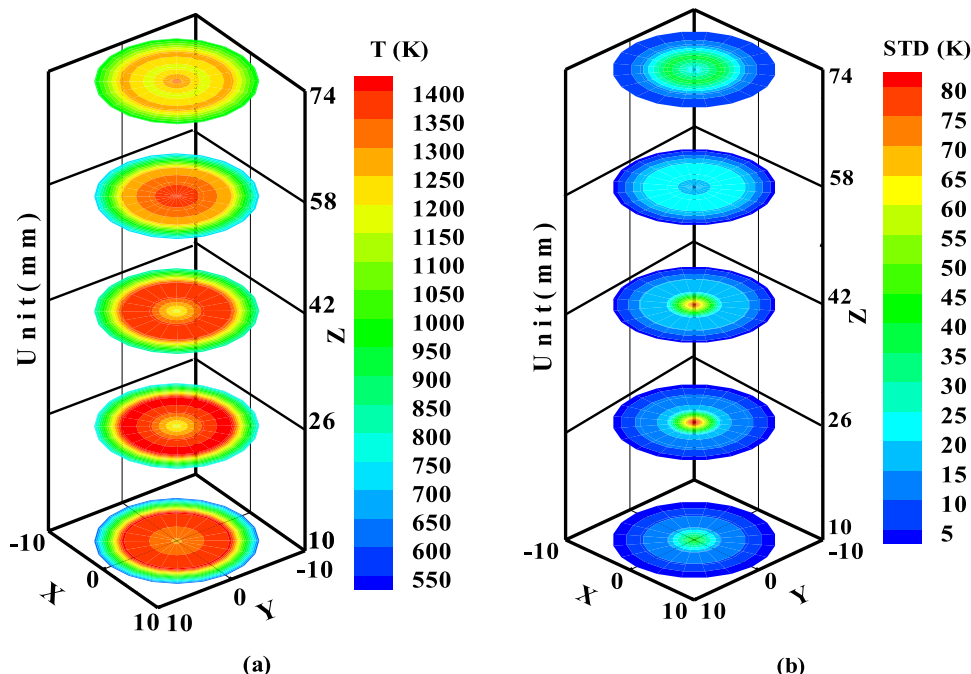


Fig. 11. Reconstructed temperature distributions and corresponding distribution of STD over the cross-sections of the flame, (a) Averaged reconstructed temperature distributions, (b) Distribution of STDs of the corresponding reconstructed temperature.

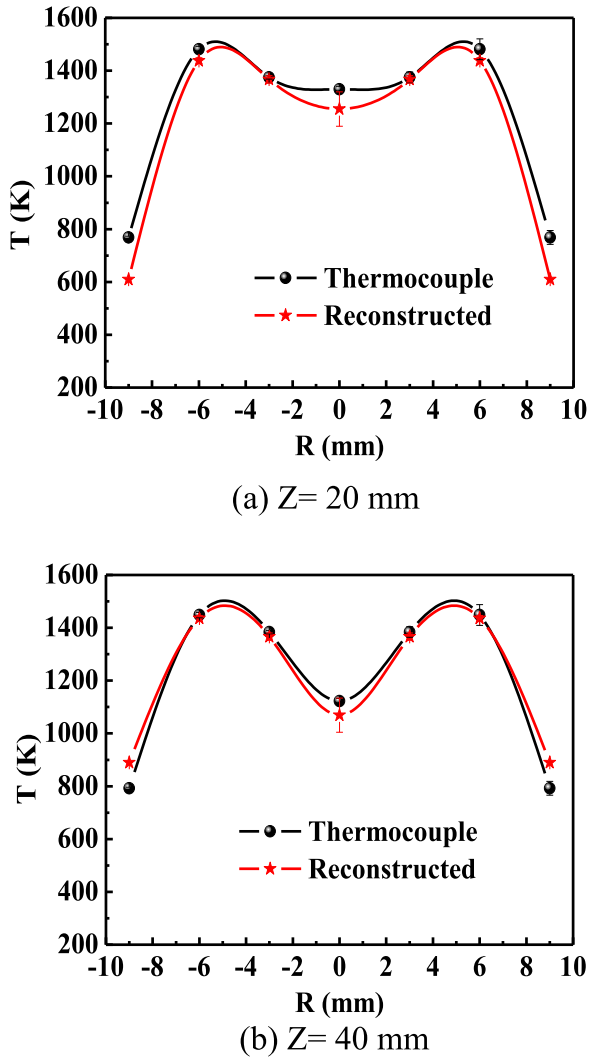


Fig. 12. Comparison of the temperatures obtained using the thermocouple and the reconstructed for seven points in radial direction at cross-sections (a) $Z=20$ mm and (b) $Z=40$ mm.

direction (along Z axis) as shown in Fig. 10. The proposed method described in Section 2.2 is utilized to reconstruct the flame temperature distribution by applying the traced rays of radiance to the flame coordinate system. The averaged reconstructed of 3-D temperature distributions and their standard deviations (STDs) distributions for the fifty images are shown in Figs. 11(a) and (b). It has been found that the measured temperature of the flame is within the range of 550–1400 K. The maximum STD has also been found 80 K. The averaged temperature of the five cross-sections have been observed 1156 K, 1167 K, 1191 K, 1157 K and 1130 K, respectively. The cross-sections from $Z=26$ mm to $Z=42$ mm of the flame have the highest temperature amongst all cross-sections. It can be seen that the highest temperature is between the center and the edge of the flame in radial direction for $Z=10$, $Z=26$ mm and $Z=42$ mm. For $Z=58$ mm and $Z=74$ mm, the highest temperature is in the center of the flame. It can also be seen that the temperature of axial voxels firstly increased and then decreased with increasing towards Z . For the radial voxels, the temperature firstly increased and then decreased with increasing R for the middle and bottom cross-sections of the flame ($Z < 58$ mm). The reconstructed 3-D temperature distributions of the flame cross-sections illustrated in Fig. 11(a) agreed well with that presented in [45].

To verify the measurement accuracy, the temperature of the flame is measured by R type high precision thermocouple. The radiation heat loss of the medium to the surroundings and the conduction heat loss of

the thermocouple bead is also considered, the temperature is corrected by using following energy balance equation [6].

$$T = \epsilon\sigma \frac{T_c^4 - T_s^4}{h_c} + T_c \quad (29)$$

where T is the actual temperature (K), T_c is the temperature measured by the thermocouple (K) and T_s is the surroundings temperature (K), h_c is the convective heat transfer coefficient ($\text{W m}^{-2} \text{K}^{-1}$) which is dependent upon gas flow conditions and the heat transfer correlation in terms of Nusselt number (Nu) defined as $h_c d/k$ (d is the diameter of the thermocouple wire and k is the gas conductivity); ϵ is the emissivity of thermocouple ($\epsilon=0.56$) and σ is Stefan-Boltzmann constant. For each measurement point, the temperature was averaged 50 readings and seven points on each cross-section were averaged. Fig. 12 illustrates the comparisons of the temperature obtained using the thermocouple and the proposed technique for the seven points in radial direction. It can be seen that the reconstructed temperature variation in radial direction is similar with the thermocouple measurement for $Z=20$ mm and $Z=40$ mm. Good agreement is observed for the both measurements. The maximum difference between the reconstructed and the thermocouple results is 75 K at $R=0$ mm and $Z=20$ mm. The difference between the two measurements may be caused by several factors in addition to the diversity of the measurement principles [5]. The relative error between the two measurements has been found no greater than 6.7%. It is clear that the proposed techniques can reconstruct the reliable and accurate 3-D temperature distribution of the flames. Since the flame temperature is reconstructed using the traced rays of radiance based on calibrated parameters (l_m, S_v, L) of the focused light field camera, the calibration error can affect the accuracy of the ray tracing and thus the temperature reconstruction of the flame.

4. Conclusions

A novel geometric calibration method has been developed to calibrate the focused light field camera. The calibration model was constructed according to the conjugate relation for camera main lens between the corner points on calibration board and their projections (virtual image points). The virtual image points from image points of raw light field image were calculated and then compared with the detected virtual image points of total focused images. The difference between them was found less than 35 pixels and this demonstrated the feasibility of the proposed method to calculate the virtual image points of the raw images. The geometric parameters of the focused light field camera based on the calibration model were obtained using Levenberg-Marquardt algorithm. The maximum mean relative error for the raw light field images is found less than 0.13%. Results obtained from the calibration demonstrated that the proposed method is capable of calibrating the geometric features of the focused light field camera. The 3-D temperature distribution of a flame was reconstructed using flame radiance and LSQR algorithm incorporating Planck's radiation law. Experiments were carried out on an ethylene air combustion test rig to reconstruct the 3-D temperature distribution of a flame. The reconstructed temperatures have been compared with that measured by thermocouple for seven representative points at two different flame cross-sections in radial distances of the flame axis. The relative error has been found no greater than 6.7% for the two measurements. Results obtained from the experiments also demonstrated that the developed methodology has provided a useful tool for reconstructing the 3-D flame temperature distributions, which is very useful for the in-depth understanding and subsequent optimization of industrial processes.

Acknowledgements

The authors wish to express their gratitude to the National Natural

Science Foundation of China (Nos. 51676044, 51327803, 51506030), the Natural Science Foundation of Jiangsu Province for Distinguished Young Scholars (No. BK20150023) and the Scientific Research Foundation of Graduate School of Southeast University for supporting the research as reported in this paper (YBJJ1605).

References

- [1] J. Ballester, T. García-Armingol, Diagnostic techniques for the monitoring and control of practical flames, *Prog. Energy Combust. Sci.* 36 (4) (2010) 375–411.
- [2] W. Cai, X. Li, F. Li, L. Ma, Numerical and experimental validation of a three-dimensional combustion diagnostic based on tomographic chemiluminescence, *Opt. Express* 21 (6) (2013) 7050–7064.
- [3] Q. Lei, Y. Wu, W. Xu, L. Ma, Development and validation of a reconstruction algorithm for three-dimensional nonlinear tomography problems, *Opt. Express* 24 (14) (2016) 15912–15926.
- [4] C. Niu, H. Qi, X. Huang, L. Ruan, H. Tan, Efficient and robust method for simultaneous reconstruction of the temperature distribution and radiative properties in absorbing, emitting, and scattering media, *J. Quant. Spectrosc. Radiat. Transf.* 184 (2016) 44–57.
- [5] Y. Yan, T. Qiu, G. Lu, M.M. Hossain, G. Gilibert, L. Shi, Recent advances in flame tomography, *China J. Chem. Eng.* 20 (2) (2012) 389–399.
- [6] M.M. Hossain, G. Lu, D. Sun, Y. Yan, Three-dimensional reconstruction of flame temperature and emissivity distribution using optical tomographic and two-color pyrometric techniques, *Meas. Sci. Technol.* 24 (7) (2013) 1–10.
- [7] D. Shi, X. Xiao, Y. He, P. Qiao, S. Chen, Measurement of three-dimensional temperature field using phase-shifting holography and CT technique, *Opt. Sci. Eng. Instrum.* 3172 (1997) 405–410.
- [8] J. Doi, S. Sato, Three-dimensional modeling of the instantaneous temperature distribution in a turbulent flame using a multidirectional interferometer, *Opt. Eng.* 46 (1) (2007) 015601-1–015601-7.
- [9] L. Ma, W. Cai, A.W. Caswell, Thilo Kraetschmer, S.T. Sanders, S. Roy, J.R. Gord, Tomographic imaging of temperature and chemical species based on hyperspectral absorption spectroscopy, *Opt. Express* 17 (10) (2009) 8602–8613.
- [10] H.N. Yang, B. Yang, X.S. CAI, C. Hecht, T. Dreier, C. Schulz, Three-dimensional (3-D) temperature measurement in a low pressure flame reactor using multiplexed tunable diode laser absorption spectroscopy (TDLAS), *Laser Eng.* 31 (2015) 285–297.
- [11] Q. Huang, F. Wang, D. Liu, Z. Ma, J. Yan, Y. Chi, K. Cen, Reconstruction of soot temperature and volume fraction profiles of an asymmetric flame using stereoscopic tomography, *Combust. Flame* 156 (3) (2009) 565–573.
- [12] Z. Yan, Q. Liang, Q. Guo, G. Yu, Z. Yu, Experimental investigations on temperature distributions of flame sections in a bench-scale opposed multi-burner gasifier, *Appl. Energy* 86 (7) (2009) 1359–1364.
- [13] P.M. Brisley, G. Lu, Y. Yan, S. Cornwell, Three-dimensional temperature measurement of combustion flames using a single monochromatic CCD camera, *IEEE Trans. Instrum. Meas.* 54 (4) (2005) 1417–1421.
- [14] Y. Gong, Q. Guo, Q. Liang, Z. Zhou, G. Yu, Three-dimensional temperature distribution of impinging flames in an opposed multiburner gasifier, *Ind. Eng. Chem. Res.* 51 (22) (2012) 7828–7837.
- [15] Z. Zhou, D. Tian, Z. Wu, Z. Bian, W. Wu, 3-D Reconstruction of flame temperature distribution using tomographic and, *IEEE Trans. Instrum. Meas.* 64 (11) (2015) 3075–3084.
- [16] W. Li, C. Lou, Y. Sun, H. Zhou, Estimation of radiative properties and temperature distributions in coal-fired boiler furnaces by a portable image processing system, *Exp. Therm. Fluid Sci.* 35 (2) (2011) 416–421.
- [17] A. Lumsdaine, T. Georgiev, “The focused plenoptic camera,” in: *Proceedings of the IEEE International Conference on Computational Photography (ICCP)*, 2009, pp. 1–8.
- [18] T. Georgiev, A. Lumsdaine, Focused plenoptic camera and rendering, *J. Electron. Imaging* 19 (2) (2010) 021106-1–021106-11.
- [19] R. Ng, M. Levoy, M. Brédif, G. Duval, M. Horowitz, P. Hanrahan, “Light field photography with a hand-held plenoptic camera, *Computer Science Technical Report CSTR of Stanford University*, 2005, pp. 1–11.
- [20] Y. Yuan, B. Liu, S. Li, H. Tan, Light-field-camera imaging simulation of participatory media using Monte Carlo method, *Int. J. Heat. Mass Transf.* 102 (2015) 518–527.
- [21] J. Sun, C. Xu, B. Zhang, M.M. Hossain, S. Wang, H. Qi, H. Tan, Three-dimensional temperature field measurement of flame using a single light field camera, *Opt. Express* 24 (2) (2016) 1118–1132.
- [22] T.W. Fahringer, B.S. Thuro, Tomographic reconstruction of a 3-d flow field using a plenoptic camera, in: *Proceedings of the 30th AIAA Aerodynamic Measurement Technology and Ground Testing Conference (AIAA)*, 2014, pp. 1–12.
- [23] S. Heber, R. Ranftl, and T. Pock, “Variational shape from light field,” *Energy Minimization Methods in Computer Vision and Pattern Recognition (EMMVCPR)*, 2013, pp. 66–79.
- [24] M. Goulet, M. Rilling, L. Gingras, S. Beddar, L. Beaulieu, L. Archambault, Novel, full 3D scintillation dosimetry using a static plenoptic camera, *Med. Phys.* 41 (8) (2014) (082101-1-082101-082113).
- [25] X. Guo, H. Lin, Z. Yu, S. McCloskey, Barcode imaging using a light field camera, *European Conference On Computer Vision (ECCV)*, 2015, pp. 519–532.
- [26] Y. Endo, K. Wakunami, T. Shimobaba, T. Kakue, D. Arai, Y. Ichihashi, K. Yamamoto, T. Ito, Computer-generated hologram calculation for real scenes using a commercial portable plenoptic camera, *Opt. Commun.* 356 (2015) 468–471.
- [27] P. Liu, R. Zhang, D. Liu, Digital depth of field control in photography based on focused plenoptic camera, in: *Proceedings of the International Conference on Intelligent Systems Research and Mechatronics Engineering*, 2015, pp. 70–75.
- [28] R. Ramachandra, K.B. Raja, C. Busch, Presentation attack detection for face recognition using light field camera, *IEEE Trans. Image Process.* 24 (3) (2015) 1060–10753.
- [29] J.T. Bolan, K.C. Johnson, B.S. Thuro, Preliminary investigation of three-dimensional flame measurements with a plenoptic camera, in: *Proceedings of the 30th AIAA Aerodynamic Measurement Technology and Ground Testing Conference (AIAA)*, 2014, pp. 1–12.
- [30] R.Y. Tsai, A versatile camera calibration technique for high-accuracy 3D machine vision metrology using off-the-shelf TV cameras and lenses, *IEEE J. Rob. Autom.* RA-3 (4) (1987) 323–344.
- [31] O.D. Faugeras, Q.T. Luong, S.J. Maybank, Camera self-calibration: Theory and experiments, *European Conference on Computer Vision (ECCV)*, 1992, pp. 321–334.
- [32] Z. Zhang, A flexible new technique for camera calibration, *IEEE Trans. Pattern Anal. Mach. Intell.* 22 (11) (2000) 1330–1334.
- [33] Y. Bok, H.G. Jeon, I.S. Kweon, Geometric calibration of micro-lens-based light-field cameras using line features, *European Conference on Computer Vision (ECCV)* pp. 47–61, 2014.
- [34] O. Johannsen, C. Heinze, B. Goldluecke, C. Perwaß, On the calibration of focused plenoptic cameras, *Time-Flight Depth Imaging* (2013) 302–317.
- [35] K.H. Strobl, M. Lingenauber, Stepwise calibration of focused plenoptic cameras, *Comput. Vis. Image Underst.* 145 (2016) 140–147.
- [36] N. Zeller, F. Quint, U. Stilla, “Calibration and accuracy analysis of a focused plenoptic camera,” *ISPRS Annals of the photogrammetry, Remote Sens. Spat. Inf. Sci.* 2 (3) (2014) 205–212.
- [37] J. Sun, C. Xu, B. Zhang, S. Wang, M.M. Hossain, H. Qi, H. Tan, Geometric Calibration of Focused Light Field Camera For 3-D Flame Temperature Measurement, in: *Proceedings of IEEE International Instrumentation and Measurement Technology Conference*, 2016, pp. 1–6.
- [38] S. Widnall, Lecture 13-vectors, matrices and coordinate transformations, *Dynamics* (2009) 1–15.
- [39] J.J. More, “The levenberg-marquardt algorithm, implementation and theory,” *Numerical analysis, Lect. Notes Math.* 630 (1977) 105–116.
- [40] J. Weng, P. Cohen, M. Herniou, Camera calibration with distortion models and accuracy evaluation, *IEEE Trans. Pattern Anal. Mach. Intell.* 14 (10) (1992) 965–980.
- [41] A. Fusiello, Elements of geometric computer vision, (http://homepages.inf.ed.ac.uk/rbf/CVonline/LOCAL_COPIES/FUSIELLO4/tutorial)
- [42] C. Niu, H. Qi, X. Huang, L. Ruan, W. Wang, H. Tan, Simultaneous reconstruction of temperature distribution and radiative properties in participating media using a hybrid LSQR-PSO algorithm, *Chin. Phys. B* 24 (11) (2015) (114401-1-114401-114411).
- [43] R. Viskanta, Concerning the definitions of the mean absorption coefficient, *Int. J. Heat. Mass Transf.* 7 (9) (1964) 1047–1049.
- [44] C. Paige, M. Saunders, LSQR: an algorithm for sparse linear equations and sparse least squares, *ACM T. Math. Softw.* 8 (1) (1982) 43–71.
- [45] S.R. Turns, *An Introduction to Combustion*, McGraw-Hill Education, New York, 1996.